ATTOSECOND DYNAMICS

Orientation-dependent stereo Wigner time delay and electron localization in a small molecule

J. Vos[1]*, L. Cattaneo[1], S. Patchkovskii[2], T. Zimmermann[3,4], C. Cirelli[1,5], M. Lucchini[1]†, A. Kheifets[6], A. S. Landsman[3,4], U. Keller[1]

Attosecond metrology of atoms has accessed the time scale of the most fundamental processes in quantum mechanics. Transferring the time-resolved photoelectric effect from atoms to molecules considerably increases experimental and theoretical challenges. Here we show that orientation- and energy-resolved measurements characterize the molecular stereo Wigner time delay. This observable provides direct information on the localization of the excited electron wave packet within the molecular potential. Furthermore, we demonstrate that photoelectrons resulting from the dissociative ionization process of the CO molecule are preferentially emitted from the carbon end for dissociative $^2\Sigma$ states and from the center and oxygen end for the $^2\Pi$ states of the molecular ion. Supported by comprehensive theoretical calculations, this work constitutes a complete spatially and temporally resolved reconstruction of the molecular photoelectric effect.

Attosecond metrology has characterized the dynamics of fundamental processes in quantum mechanics, such as the photoelectric effect in atoms. Streaking experiments and RABBITT (reconstruction of attosecond beating by interference of two-photon transitions) (1–4) have provided information on the timing of the photoionization process, known as Wigner time (τ_W) (5), defined as the energy derivative of the scattering phase ϕ_W of the electron wave packet (EWP) receding in the field of the ion: $\tau_W = \hbar \frac{\partial \phi_W}{\partial E}$, where $\hbar$ is Planck's constant h divided by 2π and E is energy. As the Wigner time delay, by its nature, is referenced to a freely propagating electron, it retrieves a photoionization time delay determined by the target-specific parameters of the scattering center (5).

At present, most photoionization time delay experiments have been performed on atomic targets [see (6) for a detailed review]. The experi-mental (7–10) and theoretical (11–14) study of molecular photoionization time delays, on the other hand, remains challenging because of the complexity of these targets. The congestion of electronic states accessible in the ionization process leads to many contributing channels of the same final energy, resulting in a multiplexed photo-electron (PE) spectrum. Additionally, molecules present a bond length–dependent spatial distribution of electron density in combination with a highly anisotropic potential landscape. This raises new questions about the angular dependence of the photoionization time delays in molecules (11, 15) and the localization of the ionizing electron within the molecule (16, 17). Recently, it has been shown that atomic photoionization time delays present a substantial angular dependence (18, 19), and a more complex angular dependence is expected for molecules because of the lower degree of symmetry. Up to now, such questions

associated with molecular targets remained un-answered because of the relative paucity of mo-lecular photoionization time delay measurements.

Extending attosecond metrology measurements to the molecular domain involves considerable experimental and theoretical challenges. Here we show that molecular attosecond measure-ments provide access not only to the orientation- and energy-dependent photoionization time delays but also to the mean position of the ionization within the molecular potential of the diatomic carbon monoxide (CO) molecule. We thereby give a complete description of the molecular photo-ionization dynamics.

A quantity specific to molecular ionization pro-cesses, the stereo Wigner time delay (SWTD) τ_{SW} (20), presents a photoionization time delay that varies depending on the location within the mo-lecular frame from which the EWP escapes.

$$\tau_{SW} = \tau_W(\text{carbon side}) - \tau_W(\text{oxygen side}) \quad (1)$$

Photoionization of the inner valence states of the CO molecule has been extensively studied in the past (21–23). In contrast to the isoelec-tronic, homonuclear N_2 molecule, the CO mole-cule is expected to show an SWTD caused by the asymmetry of the molecule's nuclear constitu-ents. This symmetry breaking provides access to a complementary observable in addition to the traditional Wigner time delay, commonly ex-tracted from attosecond pump-probe experiments. Although the Wigner time delay is specific to the molecular potential landscape, the self-referenced SWTD can be used to follow intramolecular photo-ionization dynamics on the attosecond time scale.

Identification of photoionization and dissociation channels

We ionized a supersonically expanded cold jet of CO molecules and detected the angle-resolved momenta of the (fragment) ions and electrons by using the cold target recoil ion momentum spec-troscopy (COLTRIMS) (24, 25) apparatus [see supplementary materials (SM) for details]. Photo-ionization dynamics were resolved by the interfer-ometric pump-probe RABBITT technique (26, 27), with attosecond extreme ultraviolet (XUV) pump pulses produced by high harmonic (HH) generation and a probe beam split off from the generating infrared (IR) field.

In contrast to an atomic ionization scenario, excitation energy stored in the CO^+ ion that is not released through PE emission can lead to dissociation (22). Three important ionization channels are thus accessible: the direct photo-ionization channel ($CO + h\nu \rightarrow CO^+ + e^-$, where
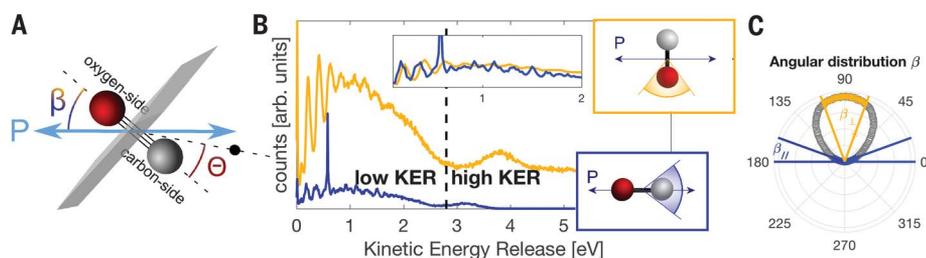

Fig. 1. KER as a function of molecular orientation. (**A**) Schematic representation of the selection based on the recoil angle with respect to the laser polarization axis P, indicated by β. The escaping side of the EWP (black) is indicated by the surface bisecting the molecular axis. (**B**) KER spectra separated in $\beta_\perp$ (orange) and $\beta_\parallel$ (blue), averaged over an angular range corresponding to an opening angle of ±20° (shaded area in blue- and orange-boxed illustrations). The inset highlights the vibrational structure observed in the low-KER (<2 eV) region. (**C**) Angular distribution of the recoil angle with respect to the field polarization axis β. The radius refers to the normalized yield. The selections of $\beta_\perp$ and $\beta_\parallel$ are highlighted in orange and blue, respectively.

ν is the photon frequency and e⁻ represents an electron) and two dissociative photoionization (DPI) channels (CO + $h\nu \rightarrow C^+ + O + e^-$ and CO + $h\nu \rightarrow O^+ + C + e^-$). Here, we focus on the DPI channel producing C^+ fragment ions.

Ideally, the photoionization dynamics would be studied in a state-resolved manner. However, the assignment of each PE-coincident (fragment) ion to an individual electronic state is generally not possible, as many states yield electrons with overlapping energy distributions due to ionization by different HHs present in the XUV spectrum. We enhanced the relative contribution of the electronic states by using angular resolution.

DPI events grant access to the recoil direction of the detected particles. This recoil frame coincides with the molecular frame when dissociation is fast compared with molecular rotation—that is, when the axial recoil approximation is valid (28). We verified that the axial recoil approximation is a valid assumption in our data treatment, with the partial exception of the $D^2\Pi$ state, which does not significantly influence the results (see SM section 3.10 for details). We thus ensured that the molecular orientation at the moment of ionization could be retrieved through the vector correlation of the detected particles (V_{C^+}, V_e, P) with respect to the laser polarization axis P without orienting the molecules (29, 30). We separated DPI events according to the recoil angle with respect to the laser polarization axis, indicated by β (Fig. 1A) and henceforth referred to as the molecular orientation. We distinguished the distribution of the kinetic energy released upon dissociation (KER) for the cases where the recoil axis is oriented perpendicular ($\beta_\perp$) or parallel ($\beta_\parallel$) to the laser polarization (orange and blue curves in Fig. 1B). The energy of the neutral O fragment is reconstructed by conservation of the total momentum sum, so that the KER is given for both nuclei involved in the fragmentation channel. We identified two regions in the KER spectrum for perpendicular orientation, characterized by low KER (<2.8 eV) and high KER (>2.8 eV) values, and designated these regions $\beta_{\perp,\text{low KER}}$ and $\beta_{\perp,\text{high KER}}$, respectively. The vibrational structure in the low KER region can be attributed mostly to the $D^2\Pi$ state, with some contributions from the $3^2\Sigma^+$ state. However, because the $D^2\Pi$ state has an SWTD of almost zero, the partial breakdown of the axial recoil approximation has a negligible effect on the measured SWTDs (for full details see section 3.10 in the SM).

The DPI evolves along various potential energy surfaces (PESs), each converging to a specific dissociation limit and fragment ion (Fig. 2A). We simulated the nuclear dissociation dynamics of individual states by using the one-dimensional quantum nonadiabatic dynamics based on the multireference configuration interaction (MRCI)/def2-TZVPP PESs and nonadiabatic couplings (see SM). The main features observed in the simulations agree with the current and previous (22, 31) experimental observations. The ratios of dissociation into the $C^+ + O$ channel for individual electronic states obtained from dissociation simulations were then combined with the photoionization cross sections to determine realistic contributions of states to RABBITT sidebands and thereby calculate SWTDs directly comparable to those in the experiment. The contributions of states to the three PE populations corresponding to $\beta_\parallel$, $\beta_{\perp,\text{low KER}}$, and $\beta_{\perp,\text{high KER}}$ determined from these simulations are summarized as follows: The PE spectrum in coincidence with recoil fragments emitted in the parallel orientation $\beta_\parallel$ is dominated by $^2\Sigma$ states, the $3^2\Sigma^+$ state at high energy and $4^2\Sigma^+$ at low energy. The PE spectrum corresponding to $\beta_{\perp,\text{low KER}}$ contains contributions from $D^2\Pi$ and $3^2\Sigma^+$ states, whereas the spectrum for $\beta_{\perp,\text{high KER}}$ is dominated by $3^2\Pi$. An energy correlation diagram showing the correlation between the KER and electron kinetic energy, and thus identifying reaction pathways (fig. S24), confirms these modeling results.

SWTD analysis

The dynamics of the photoionization are encoded in the phase of the escaping EWP, which can be retrieved by the interferometric XUV pump–IR probe technique called RABBITT (see SM) (26). In this technique, the outgoing PE, created after ionization with an XUV photon, undergoes an additional transition induced by the IR photon at the spatial and temporal overlap. Quantum path interference results in an oscillatory signal as a function of pump-probe delay τ, called a sideband (SB), which manifests between the single XUV photon absorption signals called HHs (Fig. 2B). The oscillatory signal is described by

$$\text{SB} \cong \cos(2\omega_{\text{IR}}\tau - \Delta\phi_{\text{tot}}) \cong \cos(2\omega_{\text{IR}}\tau - \Delta\phi_{\text{XUV}} - \Delta\phi_{\text{mol}}) \quad (2)$$

where ω_{IR} is the IR probe frequency. The total phase, $\Delta\phi_{\text{tot}}$, reflects the dynamic information for the escaping PE, including the attochirp of the ionizing XUV pulse ($\Delta\phi_{\text{XUV}}$) and a molecule-specific phase term, $\Delta\phi_{\text{mol}}$. The term $\Delta\phi_{\text{XUV}}$ results from the intrinsic emission delays in the HH generation process. The term $\Delta\phi_{\text{mol}}$ is characteristic of
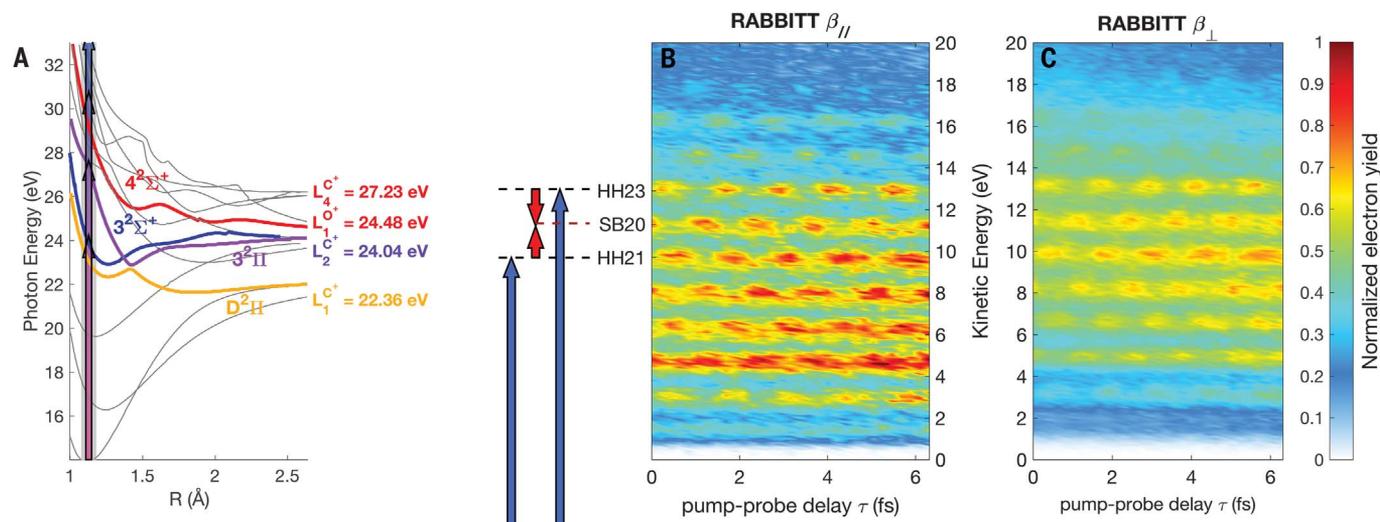

Fig. 2. Electronic states of the CO⁺ molecular ion. (**A**) PESs of the most relevant electronic states (highlighted in orange, blue and purple, and red). The CO⁺ ion dissociates after photoionization by the combined XUV and IR pulses, indicated by the arrows in the gray-shaded Franck-Condon region. The most relevant dissociation limits $L_1^{C^+}$, $L_2^{C^+}$, $L_4^{C^+}$, and $L_1^{O^+}$, adapted from (22), are indicated. R, internuclear distance. (**B**) The RABBITT trace showing the PE spectrum for molecules oriented along laser polarization, $\beta_\parallel$, recorded as a function of the pump-probe delay τ. The black and red dashed lines indicate high-order harmonics (induced by the XUV photons represented by the blue arrows) and sidebands (induced by a two-photon transition of an XUV photon and an IR photon, represented by the red arrows), respectively. (**C**) RABBITT trace for molecules with perpendicular orientation, $\beta_\perp$. Each RABBITT trace is normalized separately and does not reflect total electron counts.
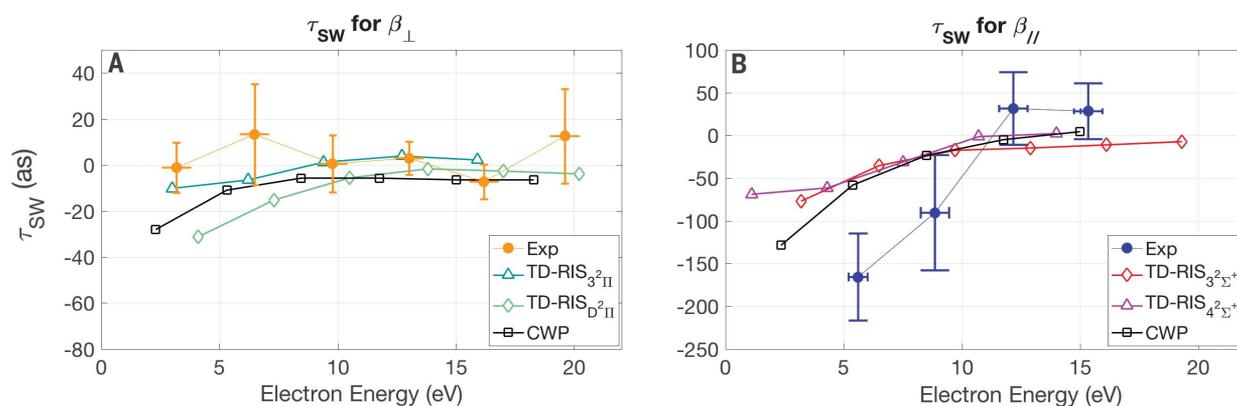
Fig. 3. Orientation- and energy-resolved SWTDs τ_{SW}. **(A)** SWTD for molecules oriented perpendicularly with respect to the laser field, integrated over the entire KER region. In this orientation the SWTDs are essentially zero within the span of the experimental error bar, which represents a combination of the 95% confidence interval for each measurement and the statistical error across all measurements weighted according to the uncertainty of the sideband fit. For a detailed analysis of the SWTDs in the low- and high-KER regions in perpendicular orientation, see fig. S24. Exp, experimental results.

(B) For parallel orientation, $\beta_{\parallel}$, a highly negative SWTD is measured at low electron energies. In this configuration, the $3^2\Sigma^+$ state is the biggest contributor at high energies; at low energies, the $4^2\Sigma^+$ state contributes substantially. The experimental results are shown in comparison with the delays obtained by theory. A direct comparison between experiment and theory based on the CWP method is possible, as the SWTDs are shown integrated over all contributing states. In contrast, state-resolved SWTDs computed by TD-RIS are shown for dominant isolated states.

the individual system and can in turn be described by the sum of two terms: $\Delta\phi_{mol} = \Delta\phi_W + \Delta\phi_{CC}$, where $\Delta\phi_{CC}$ is the measurement-induced phase term that stems from the continuum-continuum transition in the IR field (32).

The phase term of interest is the target-specific Wigner phase, $\Delta\phi_W$, described as the phase shift referenced to a free propagating EWP. The phase shift is a relative measurement; thus, the subsequent Wigner time delay, given by $\tau_W = \Delta\phi_W/2\omega_{IR}$, necessarily requires a reference. In this stereo-specific measurement we probe the photoionization dynamics associated with an intrinsic time delay in the molecule: specifically the photoionization time delay difference between PEs escaping from the carbon side versus the oxygen side. In this context an external reference is not required. Furthermore, the stereospecific measurement is insensitive to contributions from measurement-induced time delays. In particular, the attochirp contribution, $\Delta\phi_{XUV}$, cancels out in a comparison of the phase terms of sideband signals originating from the same neighboring harmonics. Additionally, assuming that the ionization probability is slowly varying with energy, $\Delta\phi_{CC}$ is removed because of the symmetric contribution of the long-range Coulomb potential (32). The stereo Wigner time is subsequently given by

$$\tau_{SW} = \frac{\Delta\phi_W(\text{carbon side}) - \Delta\phi_W(\text{oxygen side})}{2\omega_{IR}}$$

(3)

thereby yielding the absolute difference in Wigner time delay within the molecular potential.

The orientation-resolved RABBITT traces are separated according to the angle of the PE in the recoil frame (with an acceptance angle of 90°),

indicated by Θ in Fig. 1A. Each RABBITT trace is subsequently analyzed by following the procedure described in a prior work (3). Briefly, the oscillating sideband signals are integrated over an energy range of roughly 1 eV (the precise energy range is indicated by the horizontal axis in Fig. 3) and fitted to Eq. 2 after being frequency-filtered by a fast Fourier transform (see SM).

The retrieved orientation-resolved SWTDs τ_{SW} are shown in Fig. 3. For perpendicular orientation, these SWTDs are shown to be within a range of ±35 as (attoseconds) (Fig. 3A). The two KER regions are not resolved for this orientation because the KER-resolved results $\beta_{\perp,\text{low KER}}$ and $\beta_{\perp,\text{high KER}}$ yield nearly identical results (see SM). Both the experimental and theoretical curves display virtually zero or slightly positive SWTDs across all electron energies. The experimental and theoretical results are in good agreement with each other.

On the contrary, we see a clearly different behavior in the energy-dependent SWTD for the parallel orientation (Fig. 3B). The blue experimental data points show that the SWTD evolves from a negative delay difference of −165 as at ~5.0 eV to a positive value of +30 as at 14.4 eV; that is, the SWTD changes from τ_W (carbon side) < τ_W (oxygen side) to its inverse with increasing electron kinetic energy.

Interpretation of the SWTDs

To understand the highly varying SWTD for parallel orientation, we used two complementary, independent theoretical models. The first model, the time-dependent resolution in ionic states (TD-RIS) method (33, 34), describes the ionization dynamics initiated by the XUV pulse in a fully quantum mechanical manner, including the dynamics of electrons in the ion core. TD-RIS simulations do not account for the dynamics

in the IR probe field and nuclear motion. The second model, the classical Wigner propagation (CWP) method, is based on the approximate, classical propagation of the Wigner function of the PE, including the IR field. Combining the CWP method with the quantum nonadiabatic dissociation dynamics, we compute the contributions of specific states to each RABBITT sideband and thereby the photoionization time delays, which are directly comparable to the experimental results.

In the perpendicular orientation, both TD-RIS and CWP methods predict small SWTDs, as is expected for symmetry reasons. Values from both theories compare well to the experimental values, which are close to zero within the error margin.

The most notable experimental trend for $\beta_{\parallel}$, the increasing negative SWTD toward lower PE energy, is qualitatively reproduced by both theoretical models. The difference between theoretical and experimental values at lower energies may be due in part to computational constraints that prevent either theory from accounting for higher-lying states. Given the spectrum of the XUV pump pulse, the states lying above $6^2\Sigma^+$ and $9^2\Pi$, which were not considered in the theoretical treatment, may contribute only to the lowest two sidebands.

On the basis of the experimental results, we may readily conclude that the molecular photoionization delays are very sensitive to the PE emission angle Θ and the molecular orientation β. Consequently, the stereoresolved measurements of dissociative states provide a way to determine the details of the ionization process that are inaccessible to angle-integrated measurements averaged over all molecular orientations.

To obtain further insight into the highly negative SWTDs measured in parallel orientation (Fig. 3B), we calculated the Wigner functions of
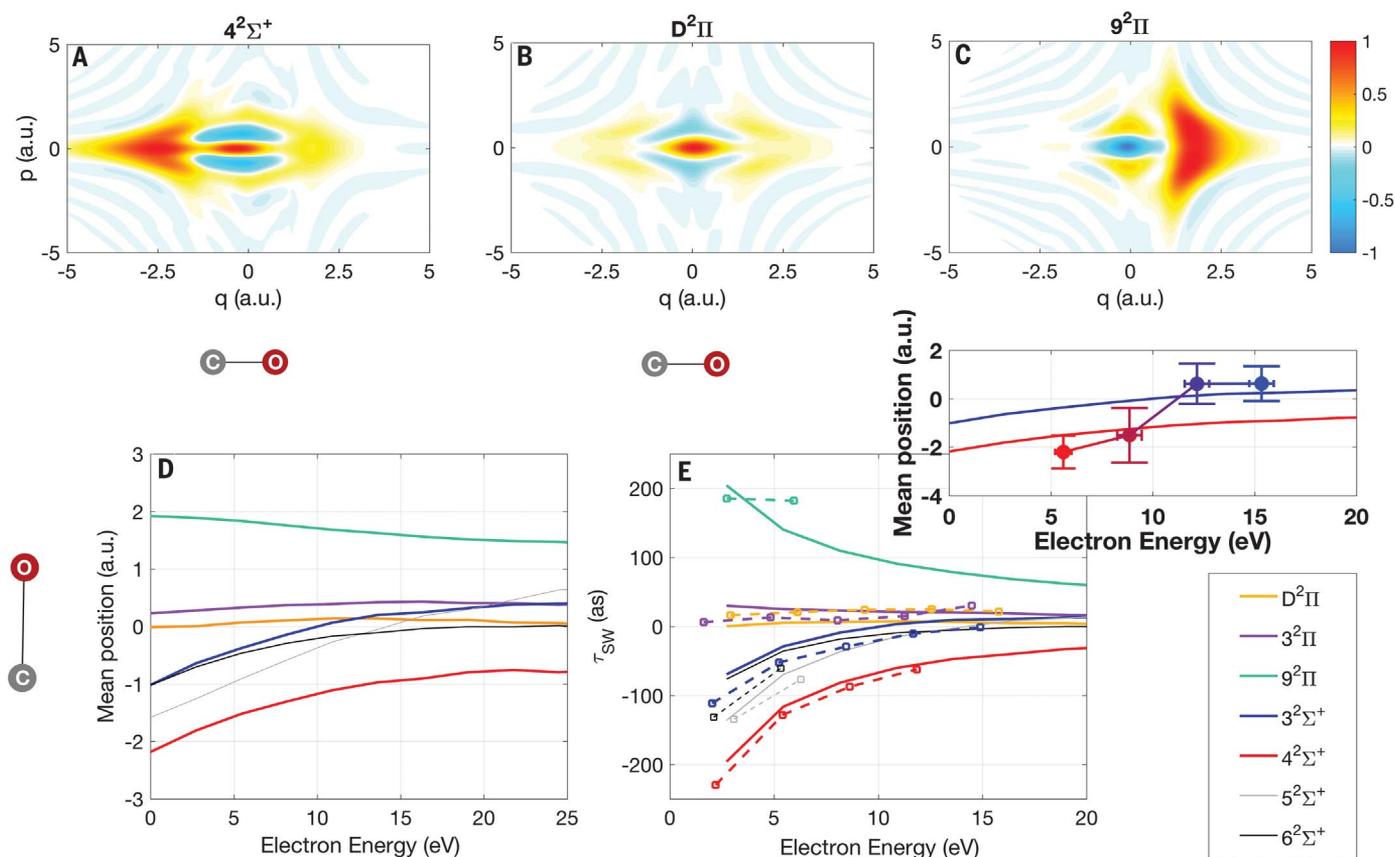
Fig. 4. SWTD and electron localization. Coordinate and momentum representations of the escaping electron at the instance of birth (provided by the source function) are shown for three representative electronic states: (**A**) $4^2\Sigma^+$, (**B**) $D^2\Pi$, and (**C**) $9^2\Pi$. The molecule is oriented parallel to the field and centered at $q = 0$, with the C side of the molecule placed on the left [C(q) = 1.07 a.u.] and the O side on the right [O(q) = 1.07 a.u.]. The $4^2\Sigma^+$ state shows a clear asymmetry along the molecular bond with a bias toward the carbon side. The $D^2\Pi$ state shows only a slight asymmetry toward the oxygen side, whereas the $9^2\Pi$ state is very strongly biased toward the oxygen side of the molecule. p, momentum. (**D**) The average electron position at the time of ionization, $q_I(E)$, as a function of electron energy for seven different states calculated by using the source functions, such as plotted in (A) to (C). (**E**) The SWTDs defined in Eq. 3 and computed for seven different states by using the CWP method (dashed lines) and $\tau_{\langle SW\rangle}$ defined in Eq. 4 and computed by using the mean position shown in (D) (solid lines). The inset shows $q_I(E)$ for the $3^2\Sigma^+$ (blue line) and $4^2\Sigma^+$ (red line) states and the experimentally extracted mean position $q_{I,exp}(E)$ (solid circles on red-blue line) for parallel-oriented molecules. The error bars represent a combination of the weighted 95% confidence interval for each measurement and the statistical error across all measurements weighted according to the uncertainty of the sideband fit.

the dipole matrix element of the Dyson orbitals for each ionization channel (Fig. 4, A to C), which we refer to as the source function (see SM). This source function provides a coordinate and momentum representation of the EWP at the instance of birth. From Fig. 4 it is clear that a large (small) asymmetry of the source function translates into a large (small) SWTD. Because the source function is symmetric with respect to the sign of the initial PE momentum, the time difference can originate from either an asymmetry in the initial localization or an asymmetry in the molecular potential experienced by the departing electron. The comparison between the SWTDs and the dipole moments of the corresponding ionic states (see SM) suggests that the asymmetry of the molecular potential is not a decisive contributor.

The asymmetry of the source function with respect to position, on the other hand, correlates

very well with the computed delays and seems to be the main factor determining the SWTD τ_{SW}. The source functions corresponding to large negative, zero, and large positive SWTDs are shown in Fig. 4, corresponding to the $4^2\Sigma^+$, $D^2\Pi$, and $9^2\Pi$ states, respectively. The $9^2\Pi$ state does not substantially contribute to the experimental RABBITT signal, and it is used only to illustrate the oxygen-leaning asymmetry that would result in large positive delays.

To show the correlation between the mean position of ionization, as computed with the CWP, and the τ_{SW} conclusively, we introduce a position interpretation of the mean SWTD

$$\tau_{\langle SW\rangle} = \frac{2q_I(E)}{\sqrt{2E}} \tag{4}$$

where E is the final kinetic energy of the ionized PE and $q_I(E)$ is the mean position of the electron at the moment of birth with respect to the geo-

metric center of the molecule. In other words, $q = 0$ identifies the midway point along the CO bond. The simple $\tau_{\langle SW\rangle}$ is independent of the details of the molecular potential experienced by the ionized PE, meaning that it depends only on the mean electron position along the molecular axis and the final electron energy (Fig. 4D). Nevertheless, $\tau_{\langle SW\rangle}$ (Fig. 4E, solid lines) shows good agreement with the SWTDs for parallel orientation calculated by the full CWP method (Fig. 4E, dashed lines).

We can conclude that at low energies, τ_{SW} shows a clear bias toward the carbon side of the molecule for all $^2\Sigma$ states considered, resulting in negative delays (Fig. 4E, inset). In particular, the $4^2\Sigma^+$ state, which shows the highest asymmetry toward the carbon side in the source function, has the most negative delays. For example, the average position of ionization $q_I(E)$ = −1.55 atomic units (a.u., where 1 a.u. is ~0.529 angstrom)

at 5 eV of electron energy suggests that the SWTD is around −120 as, which is in agreement, within the error margin, with the experimental −165 as (Fig. 4, D and E). At higher electron energies, the average electron position at birth moves toward oxygen, resulting in positive displacements, in agreement with the experimental results. On the other hand, the $^2\Pi$ states, which become relatively more important in the perpendicular orientation, show rather positive ($D^2\Pi$ and $3^2\Pi$) or highly positive ($9^2\Pi$) SWTDs. The corresponding Wigner functions show no or very small bias toward oxygen for the $D^2\Pi$ and $3^2\Pi$ states, whereas a strong bias toward oxygen is observed for the $9^2\Pi$ state.

The excellent agreement between the SWTD τ_{SW} and the delay $\tau_{\langle SW \rangle}$ (Fig. 4E) suggests that Eq. 4 can be used to infer the mean position of the ionized PE from experimental measurements alone. This quantity, $q_{I,exp}$, shown in the inset of Fig. 4, is completely independent of any fitting parameters or simulations. We show that the experimentally extracted mean position of the excited EWP, $q_{I,exp}(E)$, starts to the left of the carbon atom and quickly moves right toward the oxygen atom with increasing energy of the absorbed photon. The SWTD thereby serves as an additional source of information for molecular photoionization dynamics next to the commonly extracted Wigner time delay. In particular, in CO, the SWTD measurements allow for a straightforward extraction of the relative mean position of the ionizing electron at the moment of ionization as a function of electron energy. Therefore, measurements of the SWTD could complete the description of Einstein's photoelectric effect in molecules by adding subangstrom spatial resolution to the existing attosecond temporal resolution.

The general applicability of this method is supported by auxiliary calculations (see SM), and it is plausible that this pattern holds for larger molecules as well, particularly if final state resolution can be obtained (7, 35). Our work can serve as a benchmark not only for further experiments but also for the development of theoretical models, emphasizing the key role of the twofold dependence of the measured photoionization time delays on the molecular orientation and the intrinsic details of the molecular potential to understand more complex molecular dynamics.

REFERENCES AND NOTES

1. K. Klünder et al., Phys. Rev. Lett. **106**, 143002 (2011).
2. M. Schultze et al., Science **328**, 1658–1662 (2010).
3. L. Cattaneo et al., Opt. Express **24**, 29060–29076 (2016).
4. M. Sabbar et al., Phys. Rev. Lett. **115**, 133001 (2015).
5. E. P. Wigner, Phys. Rev. **98**, 145–147 (1955).
6. R. Pazourek, S. Nagele, J. Burgdörfer, Rev. Mod. Phys. **87**, 765–802 (2015).
7. M. Huppert, I. Jordan, D. Baykusheva, A. von Conta, H. J. Wörner, Phys. Rev. Lett. **117**, 093001 (2016).
8. S. Haessler et al., Phys. Rev. A **80**, 011404 (2009).
9. L. Cattaneo et al., Nat. Phys. 10.1038/s41567-018-0103-2 (2018).
10. C. Marceau et al., Phys. Rev. Lett. **119**, 083401 (2017).
11. P. Hockett, E. Frumker, D. M. Villeneuve, P. B. Corkum, J. Phys. B At. Mol. Opt. Phys. **49**, 095602 (2016).
12. I. A. Ivanov, A. S. Kheifets, V. V. Serov, Phys. Rev. A **86**, 063422 (2012).
13. V. V. Serov, V. L. Derbov, T. Sergeeva, Phys. Rev. A **87**, 063414 (2013).
14. V. V. Serov, A. S. Kheifets, J. Chem. Phys. **147**, 204303 (2017).
15. P. Hockett, J. Phys. B At. Mol. Opt. Phys. **50**, 154002 (2017).
16. G. Sansone et al., Nature **465**, 763–766 (2010).
17. Ch. Neidel et al., Phys. Rev. Lett. **111**, 033001 (2013).
18. C. Cirelli et al., Nat. Commun. **9**, 955 (2018).
19. S. Heuser et al., Phys. Rev. A **94**, 063409 (2016).
20. A. Chacon, M. Lein, C. Ruiz, Phys. Rev. A **89**, 053427 (2014).
21. J. H. D. Eland, E. J. Duerr, Chem. Phys. **229**, 13–19 (1998).
22. M. Lebech, J. C. Houver, D. Dowek, J. Chem. Phys. **130**, 194307 (2009).
23. M. Lebech et al., J. Chem. Phys. **136**, 094303 (2012).
24. R. Dörner et al., Phys. Rep. **330**, 95–192 (2000).
25. J. Ullrich et al., Rep. Prog. Phys. **66**, 1463–1545 (2003).
26. P. M. Paul et al., Science **292**, 1689–1692 (2001).
27. H. G. Muller, Appl. Phys. B **74**, s17–s21 (2014).
28. R. N. Zare, Mol. Photochem. **4**, 1–37 (1972).
29. M. Lebech et al., J. Chem. Phys. **118**, 9653–9663 (2003).
30. A. Lafosse et al., Phys. Rev. Lett. **84**, 5987–5990 (2000).
31. P. Baltzer et al., J. Phys. B At. Mol. Opt. Phys. **27**, 4915–4932 (1994).
32. J. M. Dahlström, A. L'Huillier, A. Maquet, J. Phys. B At. Mol. Opt. Phys. **45**, 183001 (2012).
33. M. Spanner, S. Patchkovskii, Phys. Rev. A **80**, 063411 (2009).
34. M. Spanner, S. Patchkovskii, Chem. Phys. **414**, 10–19 (2013).
35. A. E. Boguslavskiy et al., Science **335**, 1336–1340 (2012).
36. J. Vos, Orientation-dependent stereo Wigner time delay and electron localization in a small molecule, Research Collection ETH Zurich (2018); doi:10.3929/ethz-b-000259345.

Science

Orientation-dependent stereo Wigner time delay and electron localization in a small molecule

J. Vos, L. Cattaneo, S. Patchkovskii, T. Zimmermann, C. Cirelli, M. Lucchini, A. Kheifets, A. S. Landsman and U. Keller

Time and place of electron exit

Until about a decade ago, laser-induced ionization was considered instantaneous. Since then, applications of attosecond laser pulses have shown multiple subtle and complex factors that influence the precise timing of electron ejection from atoms and surfaces. Vos *et al.* measured the corresponding attosecond dynamics of dissociative photoionization in a diatomic molecule, carbon monoxide. By imaging the charged fragments, the timing could be correlated with the specific spatial portion of the molecule from which the electron wave packet emerged.

Science, this issue p. 1326